
Evidence for accumulated melt beneath the slow-spreading Mid-Atlantic Ridge

M. C. Sinha, D. A. Navin, L. M. MacGregor, S. Constable, C. Peirce, A. White, G. Heinson and M. A. Inglis

Phil. Trans. R. Soc. Lond. A 1997 **355**, 233-253

doi: 10.1098/rsta.1997.0008

Email alerting service

Receive free email alerts when new articles cite this article - sign up in the box at the top right-hand corner of the article or click [here](#)

To subscribe to *Phil. Trans. R. Soc. Lond. A* go to: <http://rsta.royalsocietypublishing.org/subscriptions>

Evidence for accumulated melt beneath the slow-spreading Mid-Atlantic Ridge

BY M. C. SINHA¹, D. A. NAVIN², L. M. MACGREGOR¹, S. CONSTABLE³,
C. PEIRCE², A. WHITE⁴, G. HEINSON⁴ AND M. A. INGLIS²

¹*Bullard Laboratories, Department of Earth Sciences, University of Cambridge,
Cambridge CB3 0EZ, UK*

²*Department of Geological Sciences, University of Durham, Durham DH1 3LE, UK*

³*Institute of Geophysics and Planetary Physics, Scripps Institution of
Oceanography, University of California San Diego, La Jolla, CA 92093, USA*

⁴*School of Earth Sciences, Flinders University of South Australia,
Adelaide 5001, Australia*

The analysis of data from a multi-component geophysical experiment conducted on a segment of the slow-spreading (20 mm yr^{-1}) Mid-Atlantic Ridge shows compelling evidence for a significant crustal magma body beneath the ridge axis. The role played by a crustal magma chamber beneath the axis in determining both the chemical and physical architecture of the newly formed crust is fundamental to our understanding of the accretion of oceanic lithosphere at spreading ridges, and over the last decade subsurface geophysical techniques have successfully imaged such magma chambers beneath a number of intermediate and fast spreading ($60\text{--}140 \text{ mm yr}^{-1}$ full rate) ridges. However, many similar geophysical studies of slow-spreading ridges have, to date, found little or no evidence for such a magma chamber beneath them.

The experiment described here was carefully targeted on a magmatically active, axial volcanic ridge (AVR) segment of the Reykjanes Ridge, centred on $57^\circ 43' \text{ N}$. It consisted of four major components: wide-angle seismic profiles using ocean bottom seismometers; seismic reflection profiles; controlled source electromagnetic sounding; and magneto-telluric sounding. Interpretation and modelling of the first three of these datasets shows that an anomalous body lies at a depth of between 2 and 3 km below the seafloor beneath the axis of the AVR. This body is characterized by anomalously low seismic P-wave velocity and electrical resistivity, and is associated with a seismic reflector. The geometry and extent of this melt body shows a number of similarities with the axial magma chambers observed beneath ridges spreading at much higher spreading rates. Magneto-telluric soundings confirm the existence of very low electrical resistivities in the crust beneath the AVR and also indicate a deeper zone of low resistivity within the upper mantle beneath the ridge.

1. Introduction

Current explanations for the mode of formation of many of the lithological and structural features observed in young oceanic crust, and in ophiolites, require the presence of an axial magma chamber at shallow depths of no more than a few kilometres below the seabed. The importance of the crustal magma chamber concept is that it

provides the setting in which the gradual crystallization of an initially primitive melt into the range of observed petrologies can occur (Sinton & Detrick 1992); it provides a reservoir from which melt can be injected into the newly forming crust as dykes or erupted onto the seafloor as lavas; and it provides a location from which deeper crustal rocks can form by a process of slow crystallization.

Geophysical observations to date have provided valuable constraints on the geometry and properties of crustal magma chambers beneath the faster spreading ridges in the Pacific (Detrick *et al.* 1987, 1993a; Collier & Sinha 1992; Harding *et al.* 1989; Vera *et al.* 1990), and have been extremely influential in the development of models for the magmatic accretion of crystalline oceanic crust at spreading rates of greater than about 60 mm yr^{-1} (Sinton & Detrick 1992; Henstock *et al.* 1993). However, there has been only one report of direct geophysical evidence for a crustal melt body beneath a slow spreading ridge (Calvert 1995). This observation relies on faint reflections seen on heavily processed multichannel seismic reflection profiles, the data from which had been previously processed and interpreted as evidence against any melt body at that location (Detrick *et al.* 1990). Numerous other geophysical experiments at a wide variety of locations on slow spreading ridges (see, for example, Fowler 1976; Fowler & Keen 1979; Purdy & Detrick 1986; Bunch & Kennett 1980; Smallwood *et al.* 1995) have failed to find evidence for a significant crustal melt body. Arguments based on thermal modelling have shown that the heat flux into the crust associated with magma delivery from the mantle is insufficient to maintain a steady-state crustal melt body, even of small dimensions, at slow spreading rates (Sleep 1975; Kuszniir & Bott 1976). This apparent contradiction between the need for crustal melt bodies to explain structural and petrological observations, and the geophysical evidence that in most places they are not present, is best resolved by the proposition that beneath slow spreading ridges, melt-filled magma chambers are transient features. If this is the case, then the process of magmatic accretion at slower spreading rates must be episodic or cyclic, and observations of crustal melt bodies will be dependent on identifying a spreading segment that is at the appropriate stage of the cycle.

In the absence of any reliable images of a crustal melt body *in situ* beneath a slow spreading ridge to date, it remains impossible to resolve important questions concerning the differences and similarities between ridge processes at different spreading rates. Of particular relevance is the question of whether accretion involves a melt body of broadly similar geometry at all spreading rates, with the major differences being confined to the temporal variability of the process (short-lived, transient melt bodies at slow rates, compared to long-lived or steady-state bodies at faster rates); or whether the geometry of the melt body, and hence the whole mechanism of crustal accretion and architecture at all scales of the crystalline crust, depends strongly on spreading rate.

In this paper we describe the results of the first integrated geophysical experiment to provide convincing evidence for a magma chamber beneath a slow spreading ridge. The experiment was centred on an AVR segment of the Reykjanes Ridge—the section of the Mid-Atlantic Ridge between the tip of the Reykjanes Peninsula on the south coast of Iceland, at $63^\circ 30' \text{ N}$, and the Charlie–Gibbs fracture zone at 52° N (inset figure 1). Our subseafloor geophysical experiment consisted of four integrated components: wide-angle seismic profiles shot to determine crustal seismic velocity structure and layer thickness; seismic reflection profiles shot to measure off-axis sediment thickness (and hopefully image crustal seismic reflectivity); controlled

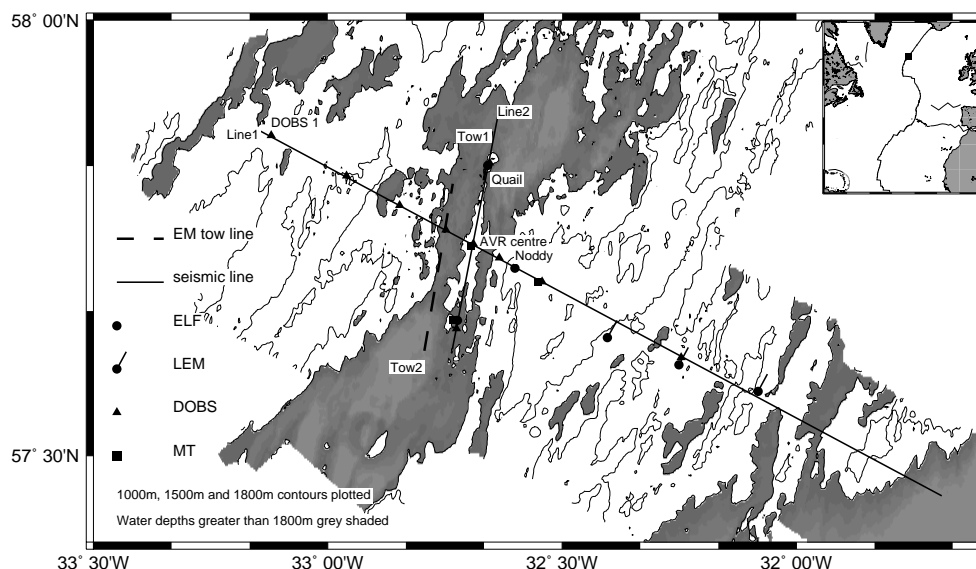


Figure 1. Experimental geometry and location. Water depths of greater than 1800 m are indicated by shading. The 1800 m bathymetric contour outlines the median valley of the ridge, and the axial volcanic ridge within the valley. Seismic (solid) and electromagnetic tow (dashed) lines are shown together with instrument locations (see key). Inset: map of the North Atlantic region showing the location of the study area.

source electromagnetic soundings to determine crustal electrical resistivity structure; and magneto-telluric soundings to investigate the deeper resistivity structure of the mantle.

2. Tectonic setting

At its northern end, the Reykjanes Ridge is profoundly affected by the proximity of the Iceland hot spot, which results in anomalously shallow water depths, the absence of a median valley and a crustal composition dominated by plume geochemistry. The hot spot influence decreases with increasing distance from Iceland, with both the geochemical and bathymetric anomalies declining steadily (Schilling *et al.* 1983; Keeton *et al.* 1997) and a discernible rift valley appearing at about 58° 40' N. The Reykjanes Ridge is segmented into a series of elongated AVRs with dimensions of up to a few tens of kilometres in length, arranged *en echelon* so that in general they overlap each other (Keeton *et al.* 1997; Searle & Laughton 1981; Searle *et al.* 1994). Individual AVRs are aligned approximately orthogonal to the spreading direction, but the overall trend of the ridge is oblique to this so that all offsets between AVR segments are right lateral. There are also no transform offsets between 57° N and the Reykjanes Peninsula—a distance of almost 950 km. Side-scan sonar imagery of the seafloor at the axis of the Reykjanes Ridge (Murton & Parson 1993) reveals a complex interplay between constructive volcanism (leading to the construction of AVRs), tectonic extension (leading to the break up of AVRs by normal faults aligned orthogonally to the spreading direction), and at distances of more than about 700 km from Iceland, the development of major inward-facing normal faults that run subparallel to the overall trend of the ridge, and form the bounding walls of the developing

median valley. Comparisons between AVRs reveal that constructive volcanism dominates at some, while at others there is little evidence of recent magmatism and tectonic features dominate. This observation leads to the inference that AVRs follow a life cycle in which occasional influxes of magma from the mantle are separated by long periods of magmatic dormancy (Parson *et al.* 1993).

The AVR chosen for the present study extends along an approximately N–S trend for some 35 km, between $57^{\circ} 33' \text{ N}$ and $57^{\circ} 53' \text{ N}$ (figure 1). Our selection was based on the assumption that the rate of melt injection into the crust (and hence the likelihood of finding a crustal melt reservoir) will be at a maximum at the point in time when the AVR is still undergoing vigorous construction. In contrast, a more mature AVR that has reached its maximum topographic development is probably already at the end of the magmatically robust phase of its life cycle. We selected, using all the available side-scan sonar and bathymetry data, the AVR which showed the greatest evidence of fresh volcanic construction (hummocky topography, bright back scattering and fresh-looking lava flows extending for distances of several kilometres), and the least evidence of the recent normal faulting and fissuring that characterizes most AVRs, and that appears to indicate post-magmatic, tectonic extension. By comparison with a number of other larger AVRs, which we interpret as being at, or close to, the end of the magmatically robust stage of their lives, our selected AVR is a relatively unimpressive feature topographically.

The site of our experiment is approximately 840 km from the Reykjanes Peninsula, and over 1100 km from the centre of the Iceland plume. At this latitude, a clear median valley is present, which extends for more than 100 km northwards towards Iceland before an axial topographic high appears. Also, as we will show in the next section, away from the axis the crustal thickness, determined seismically, is between 6 and 8 km—typical of normal Atlantic oceanic crust. We can infer from this observation that although, at the site of our experiment, the Iceland plume is close enough to cause anomalously shallow water depths and a ridge topography that is atypical of other parts of the Mid-Atlantic Ridge, it is sufficiently distant that it causes no increase in the overall rate of melt production. In §4, we will argue, based on the normal melt production rate, that what distinguishes this locality from other segments of slow-spreading ridges is not its position relative to the Iceland hot spot, but the fact that it is in the most magmatically active stage of its life cycle.

3. Experimental results

(a) *The wide-angle seismic experiment*

For the wide-angle seismic experiment we deployed an array of 11 digital ocean bottom seismometers (DOBSs) along two profiles (figure 1). Line 1 was 100 km in length and ran orthogonally to the overall trend of the Reykjanes Ridge, crossing the axis near the centre of the AVR. Line 2 was 35 km in length and ran along the AVR axis. Explosive shots at 1 or 2 km intervals and airgun shots at 100 m intervals were fired along both lines. Example explosive and airgun record sections from DOBS 1, which was located at the WNW end of line 1, are shown in figure 2*a*. The observed data from all instruments on both lines show clear crustal diving ray arrivals (Pg), while data from line 1 also show arrivals that have been refracted in the uppermost mantle (Pn).

The travel times and amplitudes of the seismic data along each profile have been analysed using synthetic seismogram modelling (figures 2*b, c*), using the ray-theory

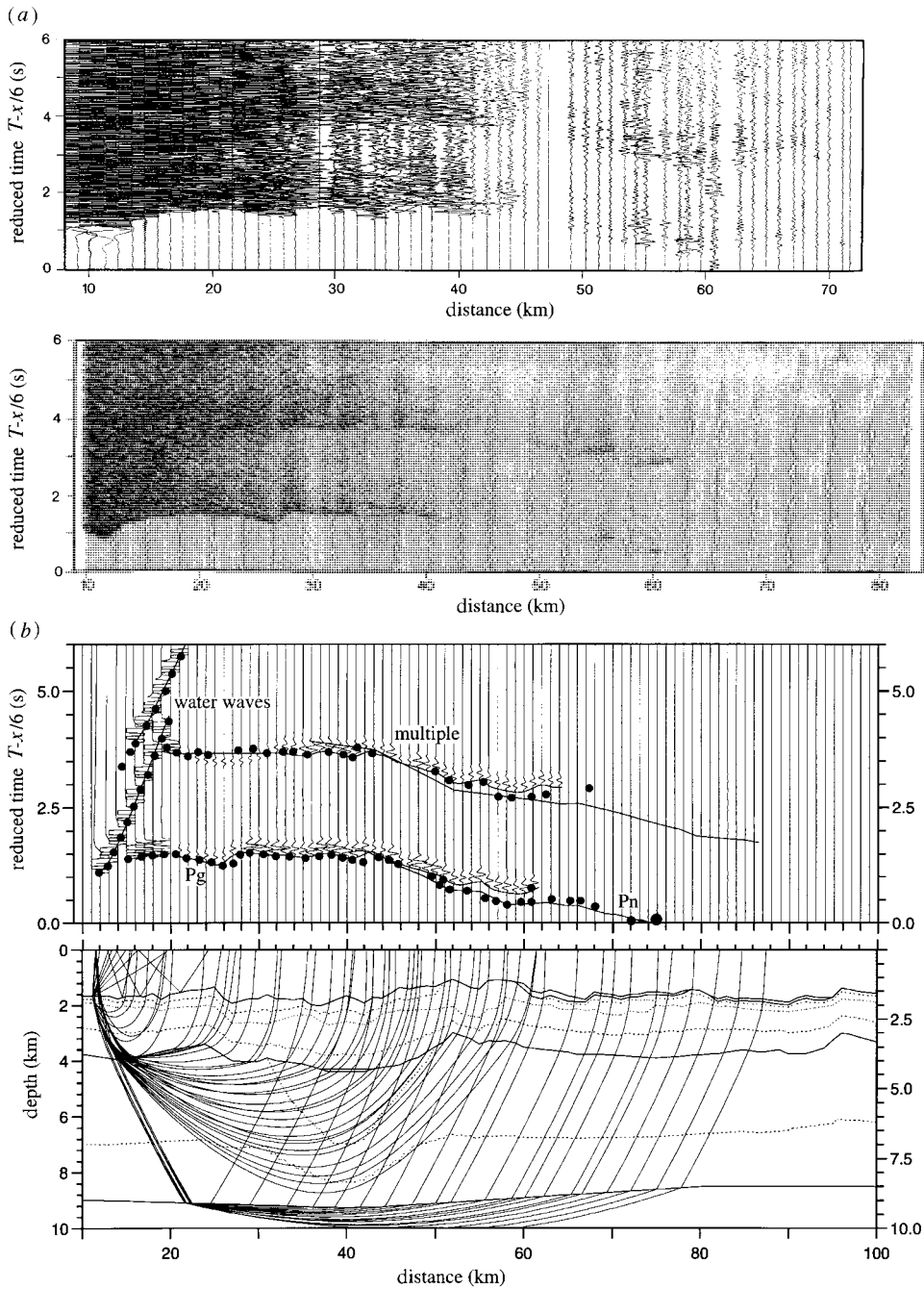


Figure 2. (a) Example explosive (upper) and airgun (lower) record sections from DOBS 1 of the wide-angle seismic experiment, showing water-borne, crustal and upper mantle arrivals. A distinct shadow zone is visible at ranges between 43 and 49 km, and is associated with the spreading axis. (b) Synthetic record section computed using the Maslov ray-theory algorithm, showing the fit of observed to synthetic data for DOBS 1. Observed travel time picks are shown by dots whose size gives an indication of the picking error. The lower panel shows a representative subset of rays used to calculate the synthetics. Dotted lines show the 4.5, 5.5, 6.0, 6.5 and 6.8 km s^{-1} isovelocity contours.

(c)

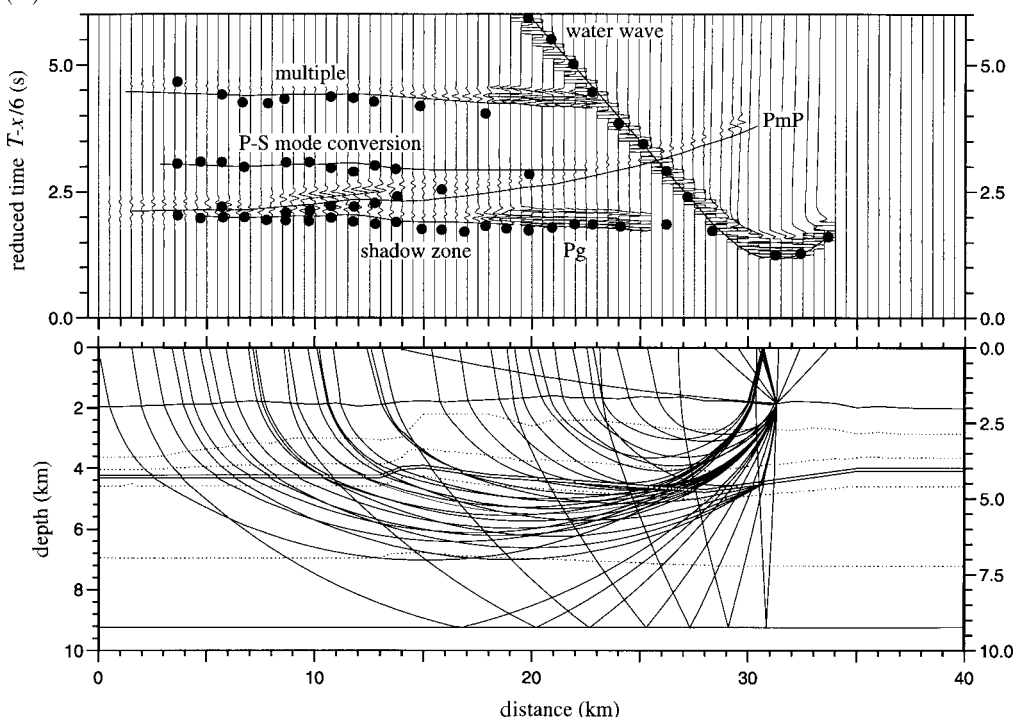


Figure 2. (c) Synthetic record section, as in (b), modelling data recorded by the DOBS located at the northern end of the along-axis line (line 2). Note the modelling of the P-wave shadow zone associated with the subaxis low-velocity body. PmP is the wide-angle reflection from the Moho discontinuity.

based Maslov algorithm (Chapman & Drummond 1982). The resulting P-wave velocity model along line 1 is shown in figure 2*d*. Both airgun and explosive record sections from all DOBSs on this profile were used to constrain the modelling. At distances of greater than 10 km from the axis, the seismic velocity structure is typical of that of normal oceanic crust (White *et al.* 1992). Beneath a thin and discontinuous layer of sediments, up to 200 m thick, the seismic velocity varies between 2.8 and 3.5 km s⁻¹ at the top of the crystalline crust. A steep velocity gradient is present in the top 2.0–2.5 km of the crust, including a change in gradient at *ca.* 500 m depth (located approximately at the 4.5 km s⁻¹ velocity contour) (Navin *et al.* 1996). The velocity reaches 6.5 km s⁻¹ at a depth of 2.0–2.5 km below the seafloor. Below this level, which we interpret as the boundary between seismic layers 2 and 3, P-wave velocity increases more slowly with depth, reaching about 7 km s⁻¹ just above the crust–mantle boundary, which occurs at between 6 and 8 km below the seabed. The uppermost mantle has a velocity of 7.9 km s⁻¹. This part of the structure is constrained primarily by travel times of lower crustal and upper mantle phases, but modelled amplitudes are also consistent with the data. Uncertainties in the model indicated by the minimum perturbations that significantly degrade the fit of synthetic to observed seismograms are typically ± 0.1 km s⁻¹ in velocity, and ± 0.5 km in depth.

The axial region has a distinctively different structure however. It is marked topographically by a shallow rift valley some 30 km wide and up to 800 m deep, within

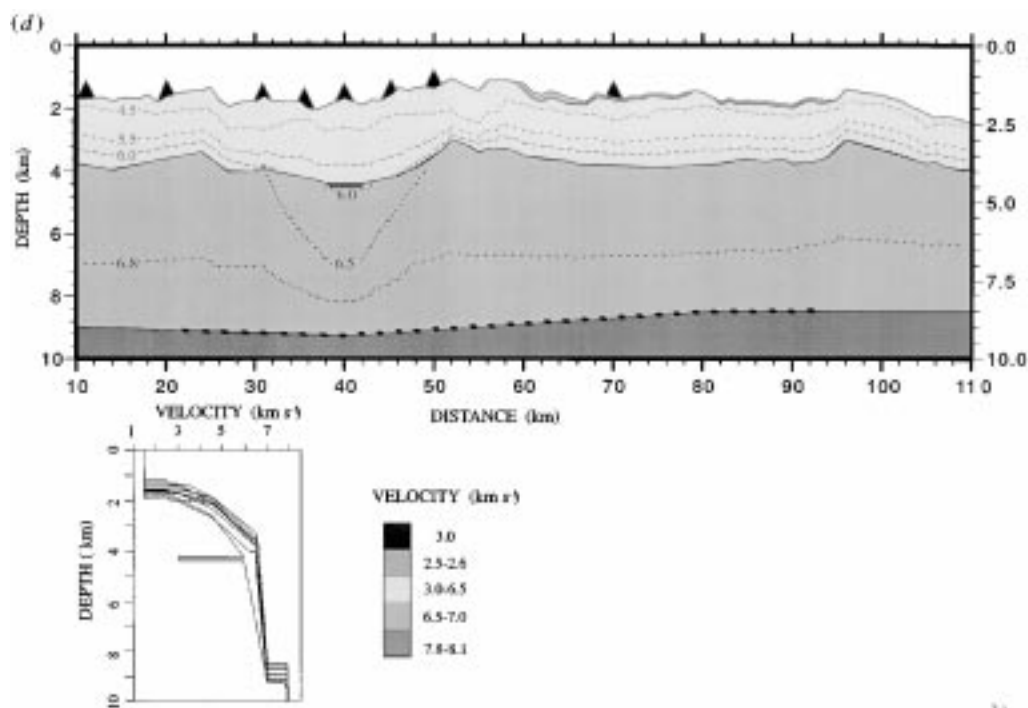


Figure 2. (d) Across-axis (line 1) seismic velocity–depth model deduced from the modelling. Contours are in km s^{-1} and DOBS positions are shown by triangles. Interfaces shown by solid lines indicate (from top to bottom): seafloor; sediment–basement boundary (where present); layer 2–layer 3 boundary; and crust–mantle boundary. The entire length of the model is constrained by many crossing ray paths. The length of the Moho constrained by the modelling is shown by the diagonal dashed line. Bottom left: velocity–depth profiles taken at intervals across the model showing crustal velocity gradients and depth to the low-velocity zone.

which lies the AVR. The walls of the valley are formed by a succession of large inward-facing normal fault scarps, which are clearly visible in swath bathymetry data collected during the experiment (Sinha *et al.* 1994; Keeton *et al.* 1997). In order to fit the travel times of crustal diving rays passing through the axial region, P-wave velocities must be depressed relative to the off-axis structure over a zone approximately 20 km wide. The seafloor velocity at the AVR is about 2.4 km s^{-1} , and crustal velocities are between 1.0 and 1.5 km s^{-1} lower than the off-axis velocities at equivalent depths throughout most of layers 2 and 3.

Perhaps the most intriguing feature of the seismic data from line 1 is the amplitude behaviour of crustal diving rays that turn at mid-crustal depths beneath the AVR axis. The amplitudes of such arrivals are anomalously low, creating prominent shadow zones on all eight record sections from the across-axis line (line 1). Unlike other variations in amplitude observed along the record sections, these anomalies cannot be explained either in terms of the velocity structure described above, or by the focusing or defocusing effects of seafloor topography. An indication of the nature of the feature that causes these shadow zones is provided by the DOBS record sections from line 2, the along-axis profile. These sections show a prominent cut-off in crustal diving ray arrivals occurring at source–receiver offsets of between 8 and 12 km. Such a feature is characteristic of a low seismic velocity zone at depth. Travel time and amplitude modelling of the data from both lines (figures 2*b, c*) has shown that a thin layer of

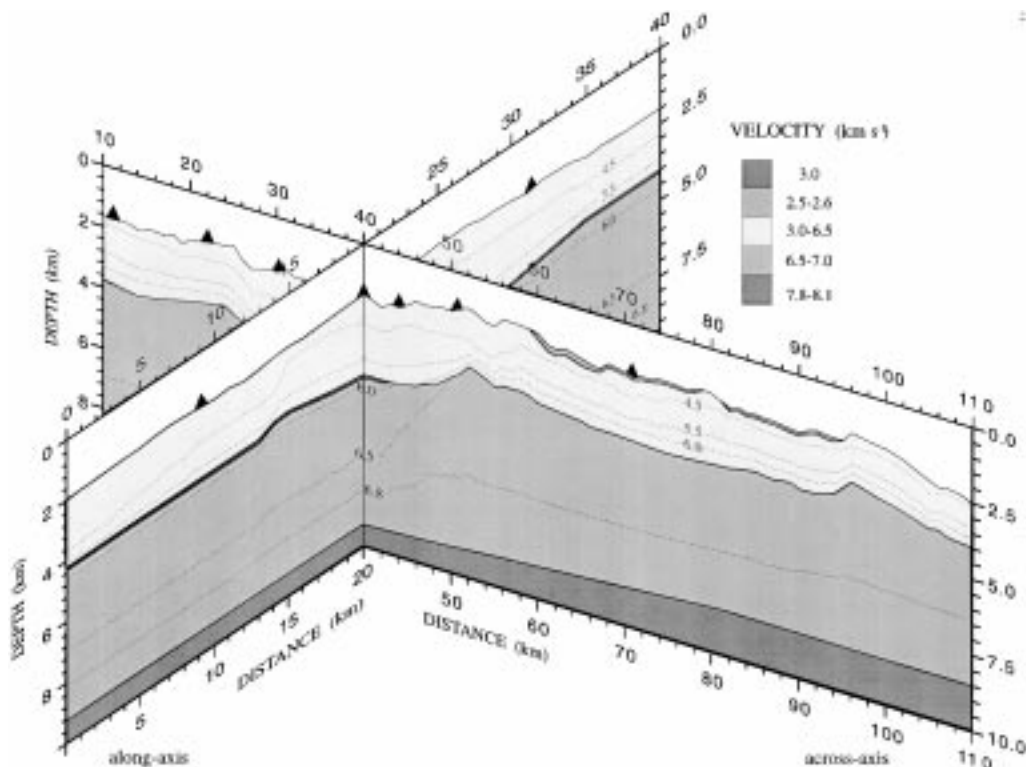


Figure 3. Final along- (line 1) and across-axis (line 2) velocity–depth models, showing the good correlation at the intersection point. DOBS locations are shown by triangles. Velocity–depth contours are in km s^{-1} . Note the limited lateral, and continuous along-axis, extent of the low-velocity body.

extremely low-velocity material is required at between 2 and 3 km depth below the axis of the AVR to explain the observed P-wave shadow zones. Only models with such a feature generate synthetic seismograms which match the observed travel times and amplitude variations with offset along both lines. In figure 2*d*, this low-velocity body is represented by a thin, lens-shaped feature, 3 km in across-axis extent, 200 m thick and with a P-wave velocity of 3 km s^{-1} . Figure 2*b* shows synthetic seismograms calculated with the Maslov code for this model while, for comparison, figure 2*c* shows synthetics calculated for the along-axis model. The velocity models independently derived by the modelling procedure for the across and along-axis profiles, lines 1 and 2, are in excellent agreement at the intersection of the two lines (figure 3).

(b) *The seismic reflection experiment*

The coincident seismic reflection data were collected simultaneously with the air-gun component of the wide-angle dataset, using an 800 m long eight-channel hydrophone streamer. The principal reason for collecting these reflection data was to measure off-axis sediment thickness, in order to provide shallow constraints on wide-angle velocity models. The 100 m shot spacing, short streamer length and consequent low stack fold, combined with the fact that the source array parameters were optimized for long-range wide-angle work, mean that the resulting data are far from ideal for observing crustal reflectivity. However, careful processing of the data from the along-axis line (line 2) has revealed a set of seismic reflections at between 3.0

and 4.0 s two-way travel time (TWTT), corresponding in depth—after allowing for variations in water depth, and using crustal velocities derived from the wide-angle data—to 2.0 to 2.5 km below the seafloor. Part of the along-axis reflection profile is shown in figure 4*a*. The travel time of the crustal reflector is much smaller than that of the first multiple of the seafloor reflection—which is calculated to arrive at much greater travel times of between 4.5 and 5.0 s, where it can indeed be observed in figure 4*a*. On the other hand, its travel times are in excellent agreement with those predicted to the low-velocity body by calculating the synthetic reflection section expected from the wide-angle velocity model along line 2. Both the TWTTs of the reflector, and the large (up to 1 s) variations in TWTT to it, are matched accurately along the entire length of the line (figure 4*b*). We therefore interpret the reflector as an intracrustal reflection from the top surface of the low-velocity body.

Amplitude modelling of this reflection event suggests that the low-velocity body may be bound by narrow gradient zones rather than distinct interfaces (figure 4*b*). However, the comparatively low data quality prevents any further quantitative analysis and investigation of this apparent contradiction with the wide-angle models. The contradiction may simply result from the limitations of the wide-angle modelling method, since it proved impossible to incorporate the gradient zone into the models and still be able to successfully ray-trace through them.

The seismic reflection profile along line 2 shows some gaps in the magma body reflection. Whether these are due to the limited data quality, or represent real along-axis discontinuities in the melt body, is unclear. Calculation of the expected reflection profile from the wide-angle model using a continuous melt body along-axis reveals that gaps in reflector continuity may be associated with severe changes in seabed topography (figure 4*b*). However, three across-axis reflection profiles, collected as part of this programme, all cross the AVR axis at points that coincide with gaps in the reflector on the along-axis profile. The reflector is not visible on any of the across-axis profiles. Thus our observations may indicate that the melt body is discontinuous along-axis within the length-scale of the AVR, but this cannot be unambiguously resolved with the currently available data.

The presence of a thin layer of very low-velocity material beneath the axis, and a larger region of more moderately depressed velocities surrounding and underlying it, is strikingly similar to the sill-like ‘melt lens’ and surrounding low-velocity zone structure that has been reported for intermediate and fast spreading ridges in the Pacific. We therefore interpret the low-velocity body as a crustal melt accumulation beneath the AVR axis. In the next two sections we will show that this interpretation is consistent with the findings obtained from the modelling of the electromagnetic data.

(c) *The controlled-source electromagnetic experiment*

The controlled-source electromagnetic (CSEM) technique involves the use of a deep-towed transmitter, which emits low-frequency continuous wave signals that are recorded by seafloor electric field recording instruments. The amplitude of the signal at the receiver provides information about the degree of attenuation of the signal during its propagation through the seafloor from source to receiver; and that in turn varies with the electrical resistivity structure of the crust. For this experiment, we deployed an array of short-arm (ELF) and long-wire (LEM) receivers (Webb *et al.* 1985) (figure 1). All of these instruments are horizontal component electric field recorders. The ELFs record two orthogonal horizontal components from a pair of

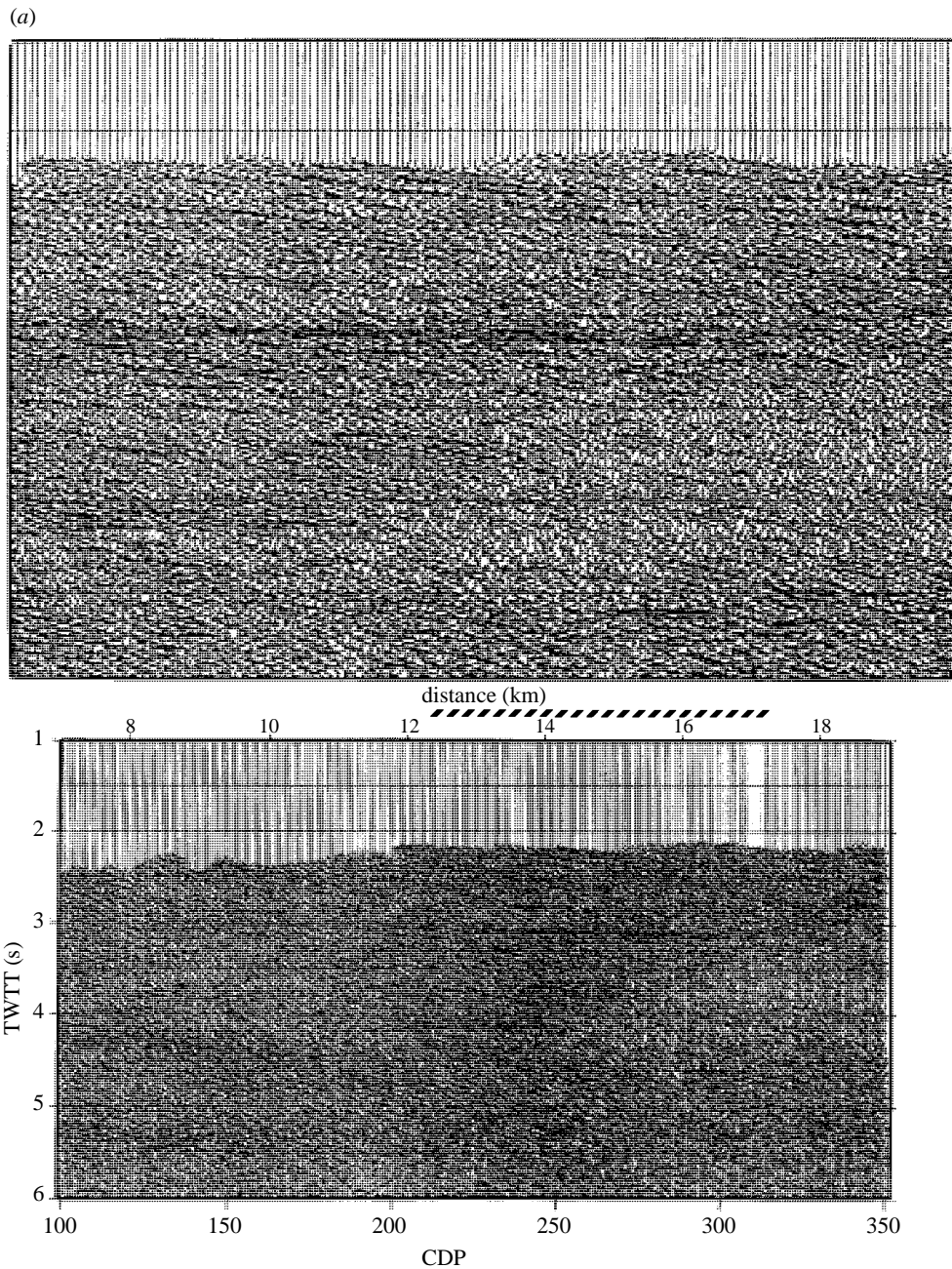


Figure 4. (a) Seismic reflection profile along line 2 (lower diagram). Note the prominent intracrustal reflection event at about 3 s TWTT, which corresponds to the thin sill-like axial low-velocity zone inferred from the wide-angle data, and which we interpret as the top surface of the axial magma chamber. The upper diagram shows an expanded view of the region denoted by the diagonal dashed line. Note how the magma chamber reflection event cross-cuts other prominent crustal reflections.

12 m dipoles, and can be used to measure signals at source-receiver ranges of up to 10–15 km. The LEMs record a single horizontal component from a 300 m dipole, and

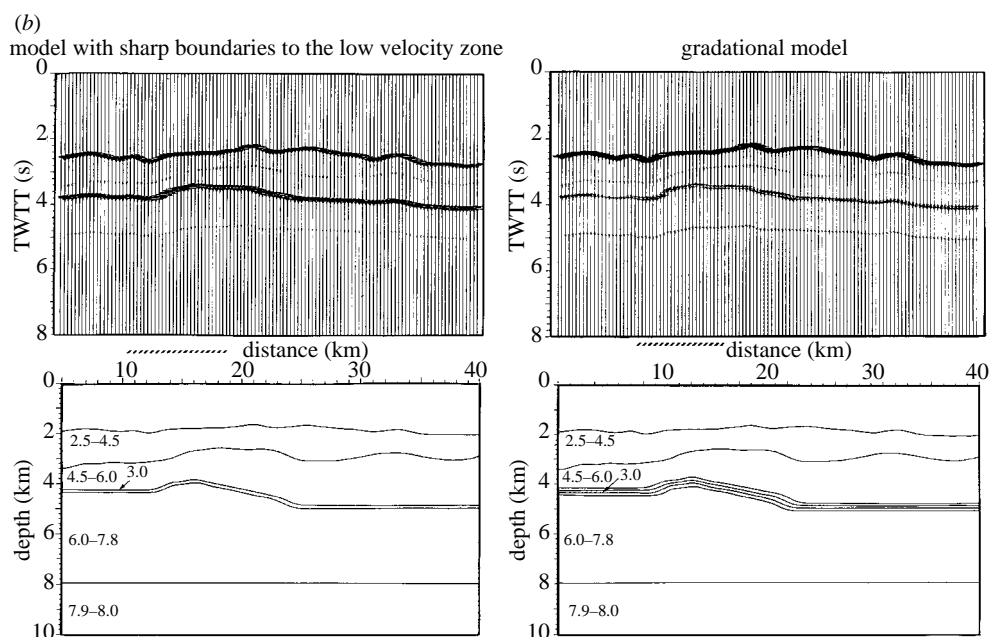


Figure 4. (b) Amplitude modelling of the magma body reflector using velocities and layer boundaries obtained from the wide-angle velocity model derived for line 2, for both a distinct upper and lower boundary (left diagram) to the low-velocity body and an upper and lower gradient zone (right diagram). Note how the gradient zone modelled amplitudes match the observed variation with distance along the profile better than those obtained using the sharp boundary model (cf. figure 5a). Layer velocities are in km s^{-1} .

can be used at source-receiver ranges of several tens of kilometres. In this paper, we will limit our analysis to the shorter range (up to 15 km) data recorded close to the axis by the ELF. Controlled-source signals were provided by the DASI deep-towed transmitter system (Sinha *et al.* 1990) along two tow lines (figure 1). Tow 1 runs along the axis of the northern part of the AVR. Tow 2 runs parallel to, and 4 km west of, the AVR. Transmission frequencies were 0.35 Hz and 11 Hz on tow 1 and 0.75 Hz on tow 2.

The best control on the shallow resistivity structure of the crust is provided by short range data. In this case, the shortest source-receiver ranges are provided by the DASI tow 1 transmissions into ELF Quail, at the northern end of the AVR. Since these data are from along-strike transmissions, as well as at short ranges (up to 4 km), they are least likely to be perturbed by lateral variations in structure, and so have been initially interpreted using a one-dimensional (resistivity varying only with depth) approach. A resistivity–depth profile derived from these data using a smooth one-dimensional Occam inversion (Constable *et al.* 1987) is shown in figure 5a, and the fit of the model to the observed data is shown in figure 5b. The inversion is unable to fit the data without some bias in the residuals—the modelled amplitudes are consistently too large for the lower frequency—and this may be due to two or possibly three-dimensional features in the true structure. However, inversions of subsets of the data—e.g. using only data from north or south of the receiver, or only one of the frequencies—yield very similar structures to the one shown, providing some confidence that the overall structure is in fact well resolved by the one-dimensional

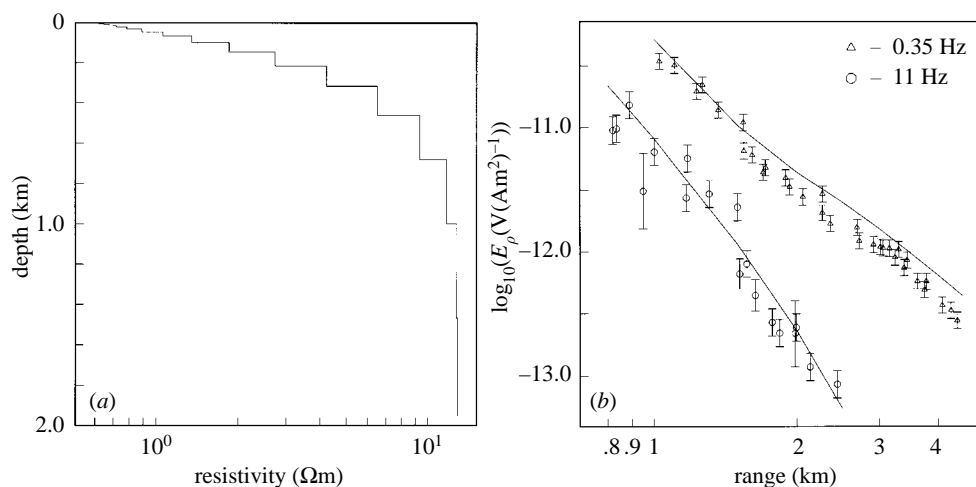


Figure 5. (a) Resistivity–depth profile for the upper part of the crust beneath the AVR axis. This structure was obtained by one-dimensional smooth inversion using the Occam algorithm of the amplitudes recorded by ELF Quail during DASI tow 1. (b) Circles and diamonds with one standard deviation error bars show the amplitudes of the $E\rho$ component of the horizontal electric field recorded by ELF Quail during transmitter tow 1, at two different frequencies. Superimposed (solid lines) are the computed $E\rho$ responses at these frequencies of the one-dimensional model shown in (a).

approximation, at least locally beneath tow 1 and down to a depth of between 1 and 2 km.

The error bars shown in figure 5b correspond to estimates of ± 1 standard deviation. Errors in this type of data arise from two sources. First, there are measurement errors arising from contamination of the receiver signal by noise, and uncertainties in source parameters (such as height above the seafloor) and source–receiver geometry. Second, there are variations in the signal amplitude due to fine scale heterogeneity in the resistivity structure close to the seafloor beneath the moving transmitter. The latter are equivalent to the ‘static shift’ errors observed in other types of electromagnetic experiment. Measurement errors of the first type can be readily quantified, and have been shown (Evans *et al.* 1994) to be smaller than the observed scatter of seafloor data. Since, in practice, it is not possible to separate the two sources of scatter in the observed data, they are both treated simply as stochastic uncertainties in the measured amplitudes. Thus the error bars shown in figure 5b represent a combination of two effects—first a contribution from genuine measurement errors, and second the influence of fine scale heterogeneity close to the transmitter, corresponding to unresolved static shift effects.

The resistivities in figure 5a are very low for crystalline rocks, ranging from 1 Ω m or less at the seabed to no more than 10–20 Ω m at 1 km depth. Both the low overall resistivity values and the steep gradient in resistivity in the top 1 km of the crust are required in order to fit the data. Such low resistivities in a basaltic crust indicate a large proportion of conductive fluid permeating the rock matrix. If we assume that, in the upper 1 km of the crust, the resistivity is primarily controlled by the penetration of sea water into fractured basalts, then these resistivities imply very high porosities (more than 10%) at the seabed, and significant porosity (at least 2%) and a highly interconnected sea water (or hydrothermal fluid) phase persisting to a depth of at least 1 km. The resistivities are lower than those found over the same depth range

at the axis of the East Pacific Rise (EPR) near 13° N (Evans *et al.* 1994), implying even higher porosities here than at the EPR.

While the model shown in figure 5*a* provides a good fit to the short range tow 1 data, it is not consistent with data observed at longer (5–15 km) ranges. The amplitudes predicted by the one-dimensional model are consistently much too low (by at least an order of magnitude) to fit the observed amplitudes at intermediate source-receiver ranges shown in figures 6*b, c*. This indicates that away from the axis, and/or at depths of greater than 1–2 km, the structure departs significantly from that shown in figure 6*a*. Attempts to invert all the data at short (figure 5*b*) and intermediate (figures 6*b, c*) ranges simultaneously using the one-dimensional approach fail to converge; while separate inversions of the three subsets of intermediate range data shown in figures 6*b, c* produce models that are all characterized by high resistivities in the upper crust, and a sharp reduction in resistivity at a depth of between 1 and 5 km.

The response of a CSEM experiment to sub-surface structure depends not only on the structure itself, but also on the experimental geometry. In the case where a horizontal electric dipole is used for both source and receiver, as here, two distinct geometric modes exist. If both dipoles are collinear, then only the radial component ($E\rho$) of the source field is seen. If the vector from source to receiver is orthogonal to both the source and receiver dipoles, then only the azimuthal component ($E\varphi$) of the source field is seen. MacGregor & Sinha (1996) have shown that, in a one-dimensional earth structure, the two modes respond very differently to the presence of a low resistivity layer at depth. In the $E\rho$ (collinear dipole geometry) case, a decrease in resistivity at depth leads to an increase in signal amplitude at moderate ranges, due to an effect that has been described as current channelling (Unsworth 1991) or a wave-guide phenomenon (Chave & Cox 1982; Chave *et al.* 1990). In the $E\varphi$ (source-receiver vector orthogonal to dipoles) case, the corresponding increase in amplitude is much smaller, or even, in some cases, absent altogether. The result of these two different behaviours is a characteristic ‘splitting’ of the $E\rho$ and $E\varphi$ amplitudes at the same range, with the $E\rho$ amplitude appearing anomalously large compared to that of $E\varphi$.

The ELF data at 5–15 km range show evidence of exactly this type of splitting. The along-axis transmissions (ELF Quail, DASI tow 2 and ELF Noddy, DASI tow 1) are dominated by the $E\rho$ component, since the source dipole is aligned parallel to the axis on both tows. The across-axis transmissions (ELF Noddy, DASI tow 2) are dominated by the $E\varphi$ component. As described above, the $E\rho$ and $E\varphi$ amplitudes are split, with the along-axis ($E\rho$) amplitudes being much larger than the across-axis ($E\varphi$) amplitudes. The split is greatest for the shortest range Noddy tow 2 data, which correspond to almost pure $E\varphi$, and diminishes as the Noddy tow 2 range increases—corresponding to an increasing $E\rho$ contribution to the signal at this instrument.

Taken together, the data indicate that any model that fits the observations must have three general features. First, the shallow structure beneath the AVR axis must be similar to that shown in figure 5*a*. Second, the overall resistivity of the crust must increase away from the axis, to explain the high amplitudes observed at 5–15 km range. Third, there must be a significant down turn in resistivity at depth beneath the axis, to account for the splitting of the $E\rho$ and $E\varphi$ component amplitudes. We have investigated the structure further by two-dimensional forward modelling, using the finite-element code of Unsworth *et al.* (1993). Figure 6*a* shows a two-dimensional model incorporating the general features described above. In addition, in order to produce a self-consistent solution that takes account of the seismic as well as the

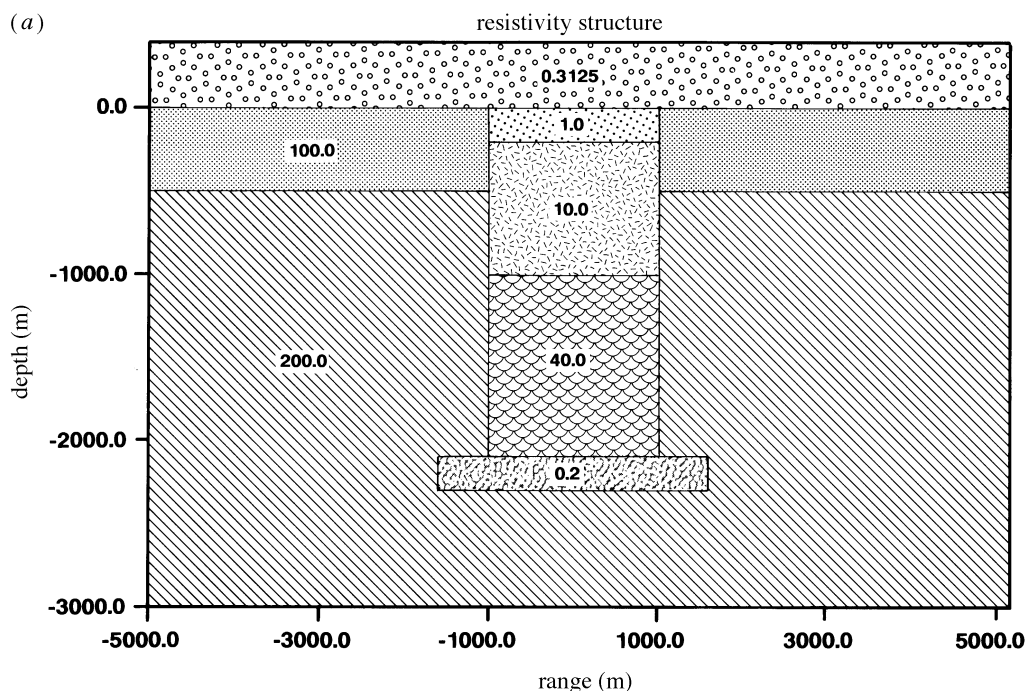


Figure 6. (a) A two-dimensional electrical resistivity model of the crust beneath the axial region, which is consistent with both the CSEM data and the structural constraints imposed by the seismic data. Note that the seismic low-velocity zone in figure 2*d* is represented here as a body with the same dimensions and location, and with an extremely low resistivity of $0.2 \Omega \text{ m}$.

electromagnetic data, the down turn in resistivity has been constrained to be in the same location, and to have the same dimensions, as the seismic low-velocity body. Figure 6*b* shows the fit of this model to the observed data. The modelled amplitudes take account of the varying source-receiver geometry in the along-strike as well as across-strike directions. It can be seen that this model provides a generally good fit, reproducing both the overall amplitudes for all source-receiver pairs, and the splitting of $E\rho$ and $E\varphi$ amplitudes. For comparison, figure 6*c* shows the fit of the same model if the low-resistivity body is not included. Although the modelled response has amplitudes that are of the same order of magnitude as the data, the splitting is not reproduced: indeed, the split in the modelled amplitudes has the wrong polarity.

Based on the modelling presented here, we conclude that the resistivity structure beneath the experiment area must be broadly similar to that shown in figure 6*a*. Very low resistivities, and a steep increase in resistivity with depth, occur in the upper 1 km of the crust beneath the AVR axis and are due to penetration of sea water or hydrothermal fluids into a highly fractured upper crust. At mid-crustal depths beneath the AVR, there is a sharp downturn in resistivity. Almost certainly this feature coincides with the seismic low-velocity zone, and is caused by a crustal magma body containing a high proportion of interconnected melt. The melt body in the model has a very low resistivity ($0.2 \Omega \text{ m}$) corresponding to the probable value for a pure basalt melt. A smaller melt body, or a similar sized body with significantly higher resistivity, is unable to reproduce the observed amplitude splitting. A larger body of slightly higher resistivity (for example, a region containing a 25% melt

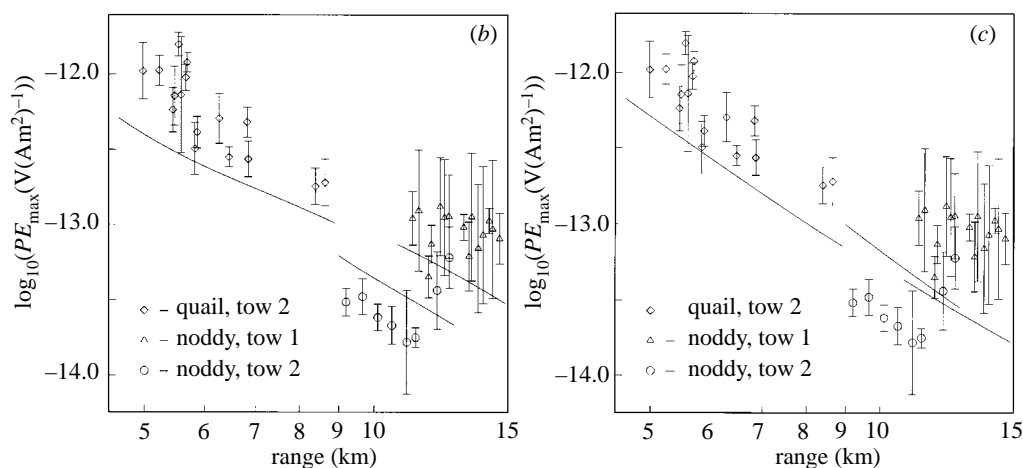


Figure 6. (b) Plot of observed amplitudes versus range for the 5–15 km range data. The amplitudes shown (circles, diamonds and triangles with one standard deviation error bars) are those of the major axis of the polarization ellipse from the two-component, short-arm instruments. Note also the much higher amplitudes of $E\rho$ (along-axis) transmissions (Quail tow 2 and Noddy tow 1), compared with $E\varphi$ (across-axis) transmissions (Noddy tow 2), at ranges greater than 5 km. This splitting of amplitudes between the two components is characteristic of a down turn in resistivity at depth. Superimposed on this figure (solid lines) are the predicted responses of the two-dimensional model shown in (a). Note the good fit of the calculated responses to the observed data, including the prominent splitting between $E\varphi$ and $E\rho$ components for ELF Noddy. The changing geometry during the two source tows results in slightly different ratios of contribution to the major axis of the polarization ellipse by the $E\varphi$ and $E\rho$ components as a function of source-receiver range, for all three source-receiver pairs. In this and other figures, the modelled responses take account of this varying geometry, which causes the small, short wavelength variations in modelled amplitudes. (c) As (b), but showing the predicted response for a model that is the same as that in (a) but does not include the low-resistivity melt lens. This model fails to reproduce the observed splitting of the $E\varphi$ and $E\rho$ components.

fraction would be expected to have resistivities of the order of 1–5 Ω m, depending on the connectivity of the melt fraction) could also fit the data. At short distances (less than 5 km) from the axis, resistivities in the upper 1–2 km of the crust must increase significantly compared to those at the axis. Longer range data from the LEM instruments indicate that further off-axis, crustal resistivities must continue to increase rapidly. Further modelling of the CSEM data is still required to define these resistivity variations in greater detail, and to incorporate the long range data from the LEM instruments.

(d) The magneto-telluric experiment

The magneto-telluric (MT) component of the experiment involved the collection of low-frequency horizontal electric field data at the centre of the AVR and at six other sites, and three-component magnetic field data at the AVR centre, its southern limit and a site 15 km east (figure 1). The source-field for the observations was provided by naturally occurring variations of Earth's magnetic field, which induce electric currents in the sea water, crust and mantle. MT impedance estimates were calculated at the latter three sites in the period range 100–10 000 s using the robust response estimation technique of Egbert & Booker (1986) using local magnetic sites for remote referencing. A combination of relatively shallow water and an energetic

period of geomagnetic activity enabled the collection of good quality data even at the shorter periods in this range.

Rotation of the MT tensor to find maximum and minimum values was effected using a tensor decomposition method (Lilley 1995). This showed a very stable orientation for the maximum value, which is coincident with the overall strike of the Reykjanes Ridge and corresponds to the TE mode. Analysis of the orthogonal, across-strike (TM) mode showed that it was not susceptible to one-dimensional inversion. Numerical modelling of the ridge suggests that this is largely due to the seafloor topography in the vicinity of the AVR, which results in electric charge accumulations on the fault scarps bounding the median valley. In addition there may be some effect due to adjacent bounding coastlines (Heinson & Constable 1992). The TE mode response is much less affected because of its alignment with the predominant geological strike of the ridge. Two-dimensional forward modelling using finite-elements (Wannamaker *et al.* 1986) suggests that the TE mode should be close to the one-dimensional response of the underlying ridge resistivity structure (Evans & Everett 1992). For the AVR centre site a one-dimensional Occam inversion (Constable *et al.* 1987) was used to obtain a smooth resistivity model beneath the AVR. Figure 7 shows the TE mode response data with error estimates, the optimum one-dimensional resistivity profile and the model response superimposed on the data. The most striking features of the data are the drop in phase at short periods (high frequencies) and the inflection in both apparent resistivity and phase at periods of 1000–3000 s. As is seen in the resulting profile, these correspond to a low-resistivity region close to the seafloor and a low-resistivity layer at depths between 50 and 100 km.

Of the features shown in the inversion in figure 7*b*, the most robust is the low-resistivity region close to the seafloor. Modelled crustal resistivities of the order of 1 to 10 Ω m are in agreement with the CSEM estimates for the top few kilometres beneath the AVR shown in figure 6*a*. The MT method lacks fine scale resolution, as skin depths are comparable to crustal thickness even at the shortest periods, but the bulk electrical properties are significant. Such a low-resistivity region is not found in similar one-dimensional inversions of TE mode data from MT sites south and east of the AVR, suggesting that it may reflect either the presence of the magma chamber beneath the AVR, or the high porosities and low resistivities in the upper 1 km of the crust beneath the AVR, or more probably the combination of both. We believe this to be the first clear evidence from seafloor MT work for the presence of conductive fluids within the crust beneath a mid-ocean ridge at any spreading rate.

A low-resistivity layer (5–10 Ω m) appears in the one-dimensional inversion over a depth range of 50–100 km. This feature is less well constrained by the TE mode data, and it is possible that it is due to two-dimensional or three-dimensional effects common to all sites. This is currently being investigated by numerical modelling. However, it is present in the inversions of data from all three MT sites (not surprisingly, since they are only 15 km apart), and persists as the data constraint is relaxed (i.e. the misfit is allowed to increase) in the smooth inversion. If it is real, it may imply a region of asthenospheric melt beneath the ridge, separated from the crust by a less conductive lithosphere which has a resistivity of more than 100 Ω m. We believe that the deeper conductive zone represents the source region of the mantle, in which adiabatic decompression of upwelling asthenosphere results in partial melting of the mantle. Assuming a highly connected melt phase within this asthenospheric layer, the inferred resistivities are consistent with a melt fraction of the order of 5%

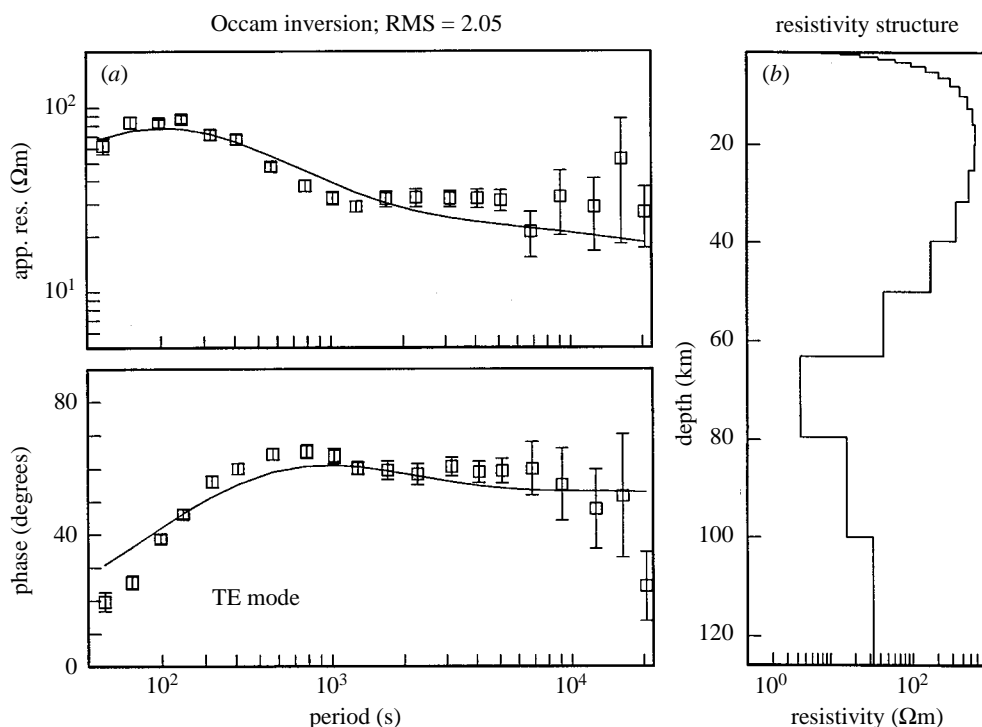


Figure 7. (a) Boxes with one standard deviation error bars show the TE mode apparent resistivity and phase responses for the MT instrument located over the centre of the AVR. Superimposed (solid lines) are the computed responses of the one-dimensional resistivity–depth model shown in (b). (b) Resistivity versus depth curve beneath the axis of the AVR, derived by one-dimensional smooth inversion of the MT data shown in (a).

(Tyburczy & Waff 1983). These results confirm the utility of MT experiments on ridges for detecting and studying mantle melting.

4. Conclusions

In combination, the geophysical results presented here provide convincing evidence for a crustal melt body beneath the AVR, represented by low seismic velocities, an intra-crustal seismic reflector, and low electrical resistivities. The MT results also provide some evidence of partial melting at deeper levels in the mantle. The most important conclusions that can be drawn from our modelling to date relate to the crustal melt body. This appears to have many broad similarities (depth below the sea surface, vertical and across-axis dimensions, and internal structure consisting of a thin, sill-like body embedded within a larger, axial low-velocity region) to those seen beneath faster spreading ridges in the Pacific. Our data are, though, unable to resolve its along-axis continuity. We conclude that the basic geometry of melt accumulation and emplacement here, beneath the slow-spreading Reykjanes Ridge, retains similar features to those at much higher spreading rates, even though the patterns of temporal and along-axis variations probably differ.

It may be argued that the Reykjanes Ridge is atypical of slow spreading ridges, owing to the influence of the Iceland plume. If this is the case, the similarities with faster spreading ridges may be unique to this location, and may not apply elsewhere.

In response to this, we would point out that while hot spot proximity may have a strong influence on some features of the ridge, such as rift valley development (Chen & Morgan 1990), the most important factor relating to the mode of emplacement of the crystalline crust is likely to be the overall flux of melt into the crust. The seismic evidence (figure 3) for normal (6–8 km) thickness crust shows very clearly that the rate of melt production here is no higher than typical values found elsewhere (away from ridge offsets) on the mid-ocean ridge system. The magmatic flux here can, therefore, be no greater than it is elsewhere on the Mid-Atlantic Ridge, where similar thickness crust is produced at the same or higher spreading rates. Other seismic experiments on the Reykjanes Ridge (Bunch & Kennett 1980; Smallwood *et al.* 1995) have failed to find any strong evidence for a crustal melt body, even though they are located closer to the Iceland hot spot, where mantle temperatures are high enough to cause some increase in overall melt production rates leading to thicker than normal crust (McKenzie & Bickle 1988). We would therefore argue that what distinguishes this locality from other segments of slow spreading ridges is not its position relative to the Iceland hot spot, but the fact that it is in the most magmatically active stage of its life cycle. Following this argument, we would expect that most AVRs on the Reykjanes Ridge—even very close to Iceland—would not be underlain by an axial melt body, since such features are short-lived and hence rare. Conversely, we would expect that other slow spreading ridge segments that, like our AVR, are at the most magmatically active stage of their life cycle, might well be underlain by comparable melt bodies, irrespective of their proximity to, or distance from, a hot spot. Hence the results of this study may be representative of the generality of slow spreading ridge segments, but only at a particular, magmatically robust stage in their magmatic-tectonic cycle.

Having identified a crustal magma body beneath a slow spreading ridge segment, an important objective for future work will be to investigate its along-axis variability—which is only poorly resolved by the experiment described here—and to relate that to the seafloor expression of crustal construction as evidenced by the morphological features of the AVR itself, and the offset discontinuities between it and adjacent spreading segments. Numerous studies of systematic along-axis variations in crustal structure and thickness at the Mid-Atlantic Ridge (see, for example, Sinha & Loudon 1983; Detrick *et al.* 1993b) have shown that the segmentation is a fundamental property of accretion, and is probably related to three-dimensional (or four-dimensional) patterns of upwelling and melt production in the underlying mantle. The outcome of this experiment encourages us to believe that, by means of careful targeting of experiments and the co-ordinated use of multiple geophysical techniques, we may in the future be able to study segmentation by direct observation of the along-axis variations in crustal magmatic structure during the magmatically active stage of a segment's life cycle.

At 2.5 km below the seafloor, the crustal melt body is at the upper end of the range of depths observed on the fast spreading East Pacific Rise (100 to 140 mm yr⁻¹), but is shallower than that observed beneath the intermediate spreading Valu Fa Ridge (Lau Basin, SW Pacific—60 mm yr⁻¹). Recent observations of apparently systematic variations in axial magma chamber depth along the East Pacific Rise have led to the suggestion that magma chamber depth may depend strongly on spreading rate (Phipps Morgan & Chen 1993). Our data refute that suggestion—the melt body is no deeper here than along parts of the East Pacific Rise which are spreading five times faster, and is shallower than at the Valu Fa Ridge, which is spreading three

times faster. Spreading rate cannot therefore be the only, or major, determinant of magma chamber depth.

Finally, the low seismic velocities and extremely low resistivities observed in the upper part of the crust imply both a high porosity and a highly connected fluid phase. In combination with the presence of a shallow crustal magma chamber, these are the conditions which would be expected to drive vigorous hydrothermal circulation systems. A systematic search of the Reykjanes Ridge axis (German *et al.* 1994) between Iceland and 58° N—terminating just north of our study area—failed to find any evidence of high-temperature venting except for the Steinaholl field, just 45 km from the Icelandic coast. It is possible, therefore, that none of the AVR segments (numbering more than 40) between Steinaholl and the 57° 43' N AVR, have experienced current or very recent magmatic activity. If this is representative of the proportion of segments that are magmatically active at a given time, it would suggest that the magmatically robust phase occupies only a small proportion (a few percent or less) of the total magmatic-tectonic life span of a slow-spreading segment.

We thank the officers and crew of RRS *Charles Darwin*, the sea-going technical staff of NERC Research Vessel Services, and other members of the scientific party of Cruise CD81, without whom the data presented in this paper could not have been collected. We also thank Roger Searle for extremely useful discussions during the selection of our target AVR, and Martyn Unsworth for the use of his two-dimensional EM code. This work was supported by the UK Natural Environment Research Council in the form of research grants, ship time and two Ph.D. studentships, by the US National Science Foundation and by the Australian Research Council.

References

- Bunch, A. W. H. & Kennett, B. L. N. 1980 The crustal structure of the Reykjanes Ridge at 59° 30' N. *Geophys. Jl R. Astr. Soc.* **61**, 141–146.
- Calvert, A. J. 1995 Seismic evidence for a magma chamber beneath the slow-spreading Mid-Atlantic Ridge. *Nature* **377**, 410–414.
- Chapman, C. H. & Drummond, R. 1982 Body wave seismograms in inhomogeneous media using Maslov asymptotic ray theory. *Bull. Seism. Soc. Am.* **72**, S277–S317.
- Chave, A. D. & Cox, C. S. 1982 Controlled electromagnetic sources for measuring electrical conductivity beneath the oceans. 1. Forward problem and model study. *J. Geophys. Res.* **87**, 5327–5388.
- Chave, A. D., Flosadottir, A. H. & Cox, C. S. 1990. Some comments on the seabed propagation of ULF/ELF electromagnetic fields. *Radio Science* **25**, 825–836.
- Chen, Y. & Morgan, W. J. 1990 Rift valley/no rift valley transition at mid-ocean ridges. *J. Geophys. Res.* **95**, 17 571–17 581.
- Collier, J. S. & Sinha, M. C. 1992 Seismic mapping of a magma chamber beneath the Valu Fa Ridge, Lau Basin. *J. Geophys. Res.* **97**, 14 031–14 053.
- Constable, S. C., Parker, R. L. & Constable, C. G. 1987 Occam's inversion: a practical algorithm for generating smooth models from electromagnetic sounding data. *Geophysics* **52**, 289–300.
- Detrick, R. S., Buhl, P., Vera, E., Mutter, J., Orcutt, J., Madsen, J. & Brocher, T. 1987 Multi-channel seismic imaging of a crustal magma chamber along the East Pacific Rise. *Nature* **326**, 35–42.
- Detrick, R. S., Mutter, J. C., Buhl, P. & Kim, I. 1990 No evidence from multichannel reflection data for a crustal magma chamber in the MARK area on the Mid-Atlantic Ridge. *Nature* **347**, 61–64.
- Detrick, R. S., Harding, A. J., Kent, G. M., Orcutt, J. A., Mutter, J. C. & Buhl, P. 1993a Seismic structure of the southern East Pacific Rise. *Science* **259**, 499–503.
- Detrick, R. S., White, R. S. & Purdy, G. M. 1993b Crustal structure of North Atlantic fracture zones. Seismic structure of the southern East Pacific Rise. *Rev. Geophys.* **31**, 439–458.

- Evans, R. L. & Everett, M. E. 1992 Magneto-tellurics and mid-ocean ridge melt transport: a two-dimensional perspective. In *Mantle flow and melt generation at Mid-Ocean Ridges* (ed. J. Phipps Morgan, D. K. Blackman & J. M. Sinton), pp. 353–361. (Geophysical Monograph 71.) Washington, DC: AGU.
- Evans, R. L., Sinha, M. C., Constable, S. C. & Unsworth, M. J. 1994 On the electrical nature of the axial melt zone at 13° N on the East Pacific Rise. *J. Geophys. Res.* **99**, 577–588.
- Egbert, G. D. & Booker, J. R. 1986 Robust estimation of geomagnetic transfer functions. *Jl R. Astr. Soc.* **87**, 173–194.
- Fowler, C. M. R. 1976 Crustal structure of the Mid-Atlantic Ridge crest at 37° N. *Geophys. Jl R. Astr. Soc.* **47**, 459–491.
- Fowler, C. M. R. & Keen, C. E. 1979 Oceanic crustal structure—Mid-Atlantic Ridge crest at 45° N. *Geophys. Jl R. Astr. Soc.* **56**, 219–226.
- German, C. R. *et al.* (11 authors) 1994 Hydrothermal activity on the Reykjanes Ridge: the Steinaholl vent-field at 63° 06' N. *Earth Planet. Sci. Lett.* **121**, 647–654.
- Harding, A. J., Orcutt, J. A., Kappus, M. E., Vera, E. E., Mutter, J. C., Buhl, P., Detrick, R. S. & Brocher, T. M. 1989 The structure of young oceanic crust at 13° N on the East Pacific Rise from expanding spread profiles. *J. Geophys. Res.* **94**, 12 163–12 196.
- Heinson, G. S. & Constable, S. C. 1992 The electrical conductivity of the oceanic upper mantle, *Geophys. J. Int.* **110**, 159–179.
- Henstock, T. J., Woods, A. W. & White, R. S. 1993 The accretion of oceanic crust by episodic sill intrusion. *J. Geophys. Res.* **98**, 4143–4161.
- Keeton J. A., Searle, R. C., Parsons, B., White, R. S., Murton, B. J., Parson, L. M., Peirce C. & Sinha, M. 1997 Bathymetry of the Reykjanes Ridge. *Mar. Geophys. Res.* (In the press.)
- Kuszniir, N. J. & Bott, M. H. P. 1976 A thermal study of the formation of oceanic crust. *Geophys. Jl R. Astr. Soc.* **47**, 83–95.
- Lilley, F. E. M. 1995 Strike direction: obtained from basic models for 3D magnetotelluric data. In *Three-dimensional electromagnetics* (ed. M. Oristaglio & B. Spies), pp. 359–369. Ridgefield, CT: Schlumberger–Doll Research.
- MacGregor, L. M. & Sinha, M. C. 1996 Marine controlled-source EM: effect of source-receiver geometry on the response of 1-D structures. Submitted to *Geophys. J. Int.* (Submitted).
- McKenzie, D. P. & Bickle, M. J. 1988 The volume and composition of melt generated by extension of the lithosphere. *J. Petrol.* **29**, 625–675.
- Murton, B. J. & Parson, L. M. 1993 Segmentation, volcanism and deformation of oblique spreading centres: a quantitative study of the Reykjanes Ridge. *Tectonophysics* **222**, 237–257.
- Navin, D. A., Peirce, C. & Sinha, M. C. 1996 Seismic evidence for a crustal magma chamber beneath the slow-spreading Reykjanes Ridge. *JAG Newsletter* **7**, 20.
- Parson, L. M. *et al.* (17 authors) 1993. En echelon axial volcanic ridges at the Reykjanes Ridge: a life cycle of volcanism and tectonics. *Earth Planet. Sci. Lett.* **117**, 73–87.
- Phipps Morgan, J. & Chen, Y. J. 1993 The genesis of oceanic crust: magma injection, hydrothermal circulation, and crustal flow. *J. Geophys. Res.* **98**, 6283–6297.
- Purdy, G. M. & Detrick, R. S. 1986 Crustal structure of the Mid-Atlantic Ridge at 23° N from seismic refraction studies. *J. Geophys. Res.* **91**, 3739–3762.
- Schilling, J. G., Zajac, M., Evans, R., Johnston, T., White, W., Devine, J. D. & Kingsley, R. 1983 Petrologic and geochemical variations along the Mid-Atlantic Ridge from 29° N to 73° N. *Am. J. Sci.* **283**, 510–586.
- Sleep, N. H. 1975 Formation of oceanic crust: some thermal constraints. *J. Geophys. Res.* **80**, 4037–4042.
- Searle, R. C. & Laughton, A. S. 1981 Fine scale sonar study of tectonics and volcanism on the Reykjanes Ridge. *Oceanol. Acta* **4**, 5–13.
- Searle, R. C., Field, P. R. & Owens, R. B. 1994 Segmentation and a non-transform ridge offset on the Reykjanes Ridge near 58° N. *J. Geophys. Res.* **99**, 24 159–24 172.
- Sinha, M. C. & Loudon, K. E. 1983 The oceanographer fracture zone. I. Crustal structure from seismic refraction studies. *Geophys. Jl R. Astr. Soc.* **75**, 713–736.

Accumulated melt beneath the slow-spreading Mid-Atlantic Ridge 253

- Sinha, M. C., Patel, P. D., Unsworth, M. J., Owen, T. R. E. & MacCormack, M. R. G. 1990 An active source electromagnetic sounding system for marine use. *Mar. Geophys. Res.* **12**, 59–68.
- Sinha, M., Peirce, C., Constable, S. & White, A. 1994 An integrated geophysical investigation of the axial volcanic region of the Reykjanes Ridge at 57° 45' N—RRS. *Charles Darwin 81 Cruise Report*, p. 39. University of Cambridge.
- Sinton, J. M. & Detrick, R. S. 1992 Mid-ocean ridge magma chambers. *J. Geophys. Res.* **97**, 197–216.
- Smallwood, J. R., White, R. S. & Minshull, T. A. 1995 Sea-floor spreading in the presence of the Iceland plume: the structure of the Reykjanes Ridge at 61° 40' N. *J. Geol. Soc.* **152**, 1023–1029.
- Tyburczy, J. A. & Waff, H. S. 1983 Electrical conductivity of molten basalt and andesite to 25 kilobars pressure: geophysical significance and implications for charge transport and melt structure. *J. Geophys. Res.* **88**, 2413–2430.
- Unsworth, M. J. 1991 Electromagnetic exploration of the oceanic crust with controlled sources. Ph.D. thesis, University of Cambridge.
- Unsworth, M. J., Travis, B. J. & Chave, A. D. 1993 Electromagnetic induction by a finite electric dipole source over a two-dimensional Earth. *Geophysics* **58**, 198–214.
- Vera, E. E., Mutter, J. C., Buhl, P., Orcutt, J. A., Harding, A. J., Kappus, M. E., Detrick, R. S. & Brocher, T. M. 1990 Structure of 0- to 0.2-m.y. old oceanic crust at 9° N on the East Pacific Rise from expanded spread profiles. *J. Geophys. Res.* **95**, 15 529–15 556.
- Wannamaker, P. E., Stodt, J. A. & Rijo, L. 1986 A stable finite element solution for two-dimensional magnetotelluric modelling, *Geophys. J. R. Astr. Soc.* **88**, 277–296.
- Webb, S. C., Constable, S. C., Cox, C. S. & Deaton, T. K. 1985 A sea-floor electric field instrument. *J. Geomagn. Geoelect.* **37**, 1115–1130.
- White, R. S., McKenzie, D. & O’Nions, R. K. 1992 Oceanic crustal thickness from seismic measurements and rare earth element inversions. *J. Geophys. Res.* **97**, 19 683–19 715.